

Measuring Shapes of Galaxy Images I: Ellipticity and Orientation

Nurur Rahman and Sergei F. Shandarin

*Department of Physics and Astronomy, University of Kansas, Lawrence, KS 66045, USA;
nurur@kusmos.phsx.ukans.edu, sergei@ku.edu*

arXiv:astro-ph/0303363v2 9 May 2003

ABSTRACT

We suggest a set of morphological measures that we believe can help in quantifying the shapes of two-dimensional cosmological images such as galaxies, clusters, and super-clusters of galaxies. The method employs non-parametric morphological descriptors known as the Minkowski functionals in combination with geometric moments widely used in the image analysis. For the purpose of visualization of the morphological properties of image contour lines we introduce three auxiliary ellipses representing the vector and tensor Minkowski functionals. We study the discreteness, seeing, and noise effects on elliptic contours as well as their morphological characteristics such as the ellipticity and orientation. In order to reduce the effect of noise we employ a technique of contour smoothing. We test the method by studying simulated elliptic profiles of toy spheroidal galaxies ranging in ellipticity from E0 to E7. We then apply the method to real galaxies, including eight spheroidals, three disk spirals and one peculiar galaxy, as imaged in the near-infrared K_s -band (2.2 microns) with the Two Micron All Sky Survey (2MASS). The method is numerically very efficient and can be used in the study of hundreds of thousands images obtained in modern surveys.

Key words: galaxies:morphology - galaxies:structure - galaxies:statistics

1 INTRODUCTION

The morphology of the objects such as galaxies, clusters, superclusters and voids of galaxies can provide important clues for understanding the past and present physical processes which play significant role in their formation. Theoretical models of the structure formation in the universe are currently based on the hierarchical clustering scenario, the most essential component of which is the idea of merging. During the evolution of the universe, small systems merge due to gravitational attraction resulting in formation of larger clumps. Merging of two or more galaxies is a violent process that significantly disturbs the shape. Hence the morphological study of galaxies and/or clusters of galaxies at present and high redshifts may reveal important information about the rate of merging at different redshifts and thus put a stringent constraints on the models of the structure formation.

The full morphological description of structures requires both topological and geometrical characteristics, and in general, is a formidable task. In practice, one would like to have as much information as possible expressed in terms of few meaningful and robust parameters as possible. This is, in principle, very difficult if not impossible to achieve. We describe and test a new method designed to quantify the shape of a two-dimensional image. We employ a set of mor-

phological measures known as Minkowski functionals (hereafter MFs). The MFs (Minkowski 1903) have already been used for detection and studies of possible non-Gaussianity in CMB maps (Schmalzing & Gorski 1998; Novikov, Feldman, & Shandarin 1999; Hobson, Jones, & Lasenby 1999; Novikov, Schmalzing, & Mukhanov 2000; Shandarin 2002; Shandarin et al. 2002) and shapes of the images of simulated clusters of galaxies (Beisbart 2000; Beisbart, Buchert, & Wagner 2001; Beisbart, Valdarnini & Buchert 2001). A subset of MFs, known as the scalar MFs, has been used for studies of three-dimensional patterns in the large-scale distribution of galaxies (Mecke, Buchert, & Wagner 1994; Schmalzing & Buchert 1997; Kerscher et al. 1997; Schmalzing et al. 1999; Kerscher et al. 2001a; Kerscher et al. 2001b; Sheth et al. 2003).

In the current study we develop a new set of quantities derived from the two-dimensions: scalar, vector and several tensor MFs, and apply them to simulated elliptic galaxies and to real galaxies as imaged in the 2MASS survey (Jarrett 2000; Jarrett et al. 2000). At present we do not make any attempt to develop a new galaxy classification. We wish to emphasize that the use of these shape descriptors could be viable along with the use of conventional structural parameters used in the galactic morphological analysis. In this

paper, we concentrate on measuring the ellipticity and orientation of the images as a function of their sizes.

It is worth noting that the MFs provide a non-parametric description of the images implying that no specific or prior assumptions are need to identify shapes. The technique is numerically very efficient and therefore is applicable to large data sets (e.g. SDSS image catalogue).

The paper is organized as follows. In Sec. 2 we give a brief introduction to the shape descriptors based on MFs and geometrical moments. Sec. 3 describes the parameters derived from the MFs to quantify shapes of simulated images. In Sec. 4 we study the effects of discreteness, atmospheric seeing, and noise. In Sec. 5 we describe a simple technique for contour smoothing and show how it reduces the distortions caused by the noise and thus improves the measurements of actual morphology. Sec. 6 discusses a few examples of the images of real galaxies from 2MASS survey. The conclusions of our investigation are summarized in Sec. 7.

2 MINKOWSKI FUNCTIONALS AS SHAPE DESCRIPTORS

The MFs consist of a set of measures carrying both the geometric (e.g. areas, perimeters) and topological (the Euler characteristic) information about the image. The MFs obey a set of covariance properties such as motion invariance, additivity and continuity. Here we use the scalar, vector and a selection of tensor MFs. The quantitative characteristics of images described below can be also characterized as geometric moments, e.g. (Mukundan & Ramakrishnan 1998). We use the so called silhouette and boundary moments up to second order.

2.1 Scalar MFs

There are three scalar MFs derived from two dimensions: the area (A), perimeter (P), and the Euler characteristic (EC, χ) of any region specified by a contour (e.g. isophotal contour)

$$A = \int_K da, \quad (1)$$

$$P = \oint dl, \quad (2)$$

$$\chi = \frac{1}{2\pi} \oint \kappa dl, \quad (3)$$

where $\kappa = 1/R$ is the curvature of the contour, and K is the region bounded by a given contour. For all simply connected regions $\chi = 1$ and therefore is not used in the paper. Note also, that in cosmological studies of two dimensional fields the genus is often used instead of EC. The genus and EC are uniquely related and thus carry exactly the same information. The three scalar moments are translationally and rotationally invariant and thus do not carry any directional information. The scalar MFs can be considered as three geometric moments of zeroth order.

2.2 Vector MFs

Three vector MFs defining three centroids: the center of the area (A_i), the center of contour (P_i), and the center of curvature (χ_i) are given as follows

$$A_i = \frac{1}{A} \int_K x_i da, \quad (4)$$

$$P_i = \frac{1}{P} \oint x_i dl, \quad (5)$$

$$\chi_i = \frac{1}{2\pi} \oint x_i \kappa dl. \quad (6)$$

The vector MFs are in fact the center of mass (A_i) of the region within the contour assuming that the surface density is constant, center of mass of the homogeneous contour (P_i), and center of mass of the contour (χ_i) having the linear density that equals the curvature κ . Three centroids obviously coincide with each other in the case of centrally symmetric images but are generally different if the central symmetry is broken. The centroids are the geometrical moments of the first order carrying directional information.

2.3 Tensor MFs

Out of many tensor MFs e.g. (Beisbart 2000) we use only the following three central moments of the second order

$$A_{ij} = \int_K (x_i - A_i)(x_j - A_j) da, \quad (7)$$

$$P_{ij} = \oint (x_i - P_i)(x_j - P_j) dl, \quad (8)$$

$$\chi_{ij} = \frac{1}{2\pi} \oint (x_i - \chi_i)(x_j - \chi_j) \kappa dl. \quad (9)$$

The tensors A_{ij} , P_{ij} and χ_{ij} (also known as the curvature tensor) are closely related to the inertia tensors of a homogeneous region, a homogeneous contour, and a contour weighted by the curvature, κ , respectively. The three sets of moments provide the lowest order geometrical characteristics of the image including its orientation.

2.4 Ellipse

Galaxy samples indicate environment dependent number density of galaxies of different morphologies: elliptic, spirals, and irregular/peculiar types. In morphological studies of galaxies, a conventional method is to approximate a galaxy shape by an ellipse (Carter & Metcalfe 1980). Since the ellipse fitting technique is well known and widely used, to get a better feeling of the MFs we think it would be useful to begin with an analytical calculation of the MFs of an ellipse. Let us consider the equation of an ellipse centered at the origin

$$\frac{x^2}{a^2} + \frac{y^2}{b^2} = 1, \quad (10)$$

where a and b are the semi-axes ($b \leq a$). Then, the scalar MFs are

$$A^{ell} = \pi ab, \quad P^{ell} = 4aE(e), \quad \chi^{ell} = 1, \quad (11)$$

where $e = \sqrt{1 - b^2/a^2}$ is the eccentricity of the ellipse, $E(e) = \int_0^{\pi/2} (1 - e^2 \sin^2 \psi)^{1/2} d\psi$ is the complete elliptic integral of the second kind. Due to central symmetry of the ellipse its vector MFs coincide with the center of symmetry of the ellipse: $A_i = 0$, $P_i = 0$, and $\chi_i = 0$.

The eigen values of the tensor MFs are respectively

$$A_{xx}^{ell} = \frac{\pi}{4} ab^3, \quad A_{yy}^{ell} = \frac{\pi}{4} a^3 b \quad (12)$$

$$\begin{aligned} P_{xx}^{ell} &= \frac{4}{3} a^3 \frac{(1 - e^4)E(e) - (1 - e^2)^2 K(e)}{e^2}, \\ P_{yy}^{ell} &= \frac{4}{3} a^3 \frac{(1 - e^2)K(e) - (1 - 2e^2)E(e)}{e^2}, \end{aligned} \quad (13)$$

$$\chi_{xx}^{ell} = \frac{b^3}{a + b}, \quad \chi_{yy}^{ell} = \frac{a^3}{a + b}. \quad (14)$$

Here $K(e) = \int_0^{\pi/2} (1 - e^2 \sin^2 \psi)^{-1/2} d\psi$ is the complete elliptic integral of the first kind.

3 METHOD

We treat an image as a set of contour lines built from a pixelized map. First, we construct a contour at every chosen level by using the linear interpolation technique described in (Shandarin et al. 2002). The contour is represented by an ordered set of points. In addition to the coordinates of each contour point the angles between the adjacent segments are also used as they carry information about the curvature of the contour.

The measurements provide three scalar (eq. 1 - 3), three centroids (eq. 4 - 6) and a total nine components of the tensor MFs (eq. 7 - 9). In order to make representation more homogeneous and intuitive we transform the tensor MFs into pairs of parameters: one of which is the area and the other is the perimeter of the ellipse having exactly the same tensor MFs.

For instance, consider the tensor P_{ij} (eq. 8). First, we find the eigen values of the tensor and insert them into eqs. 13. Then, solving these equations for a and e we find the parameters of an ellipse (e.g. the semi-axes a_P , b_P) having exactly same tensor P_{ij} as obtained for the contour in question. For brevity we shall call this auxiliary ellipse the perimeter ellipse (compare to the image ellipses in (Mukundan & Ramakrishnan 1998)). We characterize the perimeter ellipse by its area A_P and perimeter P_P which are calculated by inserting a_P and b_P in eq. 11. Figure 1 illustrates this procedure: in every panel the solid line shows the contour while the dashed line shows the auxiliary perimeter ellipse having exactly the same P_{ij} as the contour itself and the orientation of its largest axis is orthogonal to the orientation of the largest axis of the P_{ij} tensor (eq. 8).

Similarly the tensors A_{ij} and χ_{ij} are represented by the area and curvature ellipses which are characterized by the pairs A_A, P_A and A_χ, P_χ respectively and are shown in Fig. 1 by dotted and dashed-dotted lines. The orientations of the auxiliary ellipses are marked by the orientations of the corresponding largest axes in Fig. 1.

Summarizing the previous description we present the list of the parameters characterizing a contour

- three vectors A_i, P_i , and χ_i (eqs. 4 - 6) defining the centroids of the area, perimeter and curvature ellipses which coincide with the corresponding centroids of the region and contour themselves;

- four areas: the area within the contour itself A_S (subscript S indicates that it is one of the scalar MFs) and the areas of the auxiliary ellipses: A_A , A_P and A_χ ;

- four perimeters: the perimeter of the contour itself P_S and the perimeters of the auxiliary ellipses P_A , P_P and P_χ ;

- three angles showing the orientation of the three auxiliary ellipses.

In the ideal case of perfect measurements of a perfect ellipse all the estimates would be the same: the areas of all auxiliary ellipses are equal to the area of the contour itself ($A_S = A_A = A_P = A_\chi = A_{cont}$) as well as the perimeters of the are equal to the auxiliary ellipses are equal to the perimeter of the contour itself ($P_S = P_A = P_P = P_\chi = P_{cont}$). In addition, all three vectors are the same ($A_i = P_i = \chi_i$) as well as the orientations of all auxiliary ellipses. This is illustrated by panels 1 and 2 in Fig. 1 where all three auxiliary ellipses are on top of each other and overlap with the contour itself.

However, if the contour is not elliptic, all the auxiliary ellipses are in general different. The use of the auxiliary ellipses effectively relates the contour to an ellipse: the similarity of three auxiliary ellipses is a strong evidence that the shape of the contour is elliptic. It is worth emphasizing that the plots of the auxiliary ellipses are used only for illustrative purpose, the quantitative analysis of the images is based on the computation and comparison of their parameters. In our analysis we compute the parameters for a set of levels and plot them as a function of the area within the contour.

3.1 Toy Examples

In order to develop a better feeling how the parameters defined in the previous section characterizing the shape of various contours we briefly discuss nine different contours shown in Fig. 1.

In the first two panels all three auxiliary ellipses coincide with the contour itself indicating that the both contours (a circle in panel 1 and ellipse in panel 2) are true ellipses. In the seven remaining panels the auxiliary ellipses are all different. In most cases the area ellipse (dotted lines) is the smallest and the curvature ellipse (dashed-dotted lines) is the largest of the three.

The vector MFs mark the centers of the corresponding auxiliary ellipses and are shown by the open square, circle and star corresponding to the area (eq. 4), perimeter (eq. 5) and EC (eq. 6) vectors MFs respectively. If the contour has a center of symmetry then all three points coincide with it (panels 1 through 5). In the case of mirror symmetry of a contour they lie on the axis of the symmetry (panels 6, 7 and 8). The mirror symmetry also results in a similar orientation of all ellipses.

Finally, an asymmetric and irregular contour generally results in three auxiliary ellipses with different sizes and orientations. This is illustrated in panel 9 which shows one real galaxy contour constructed form a 2MASS image of the peculiar galaxy NGC4485. Note that in addition to being

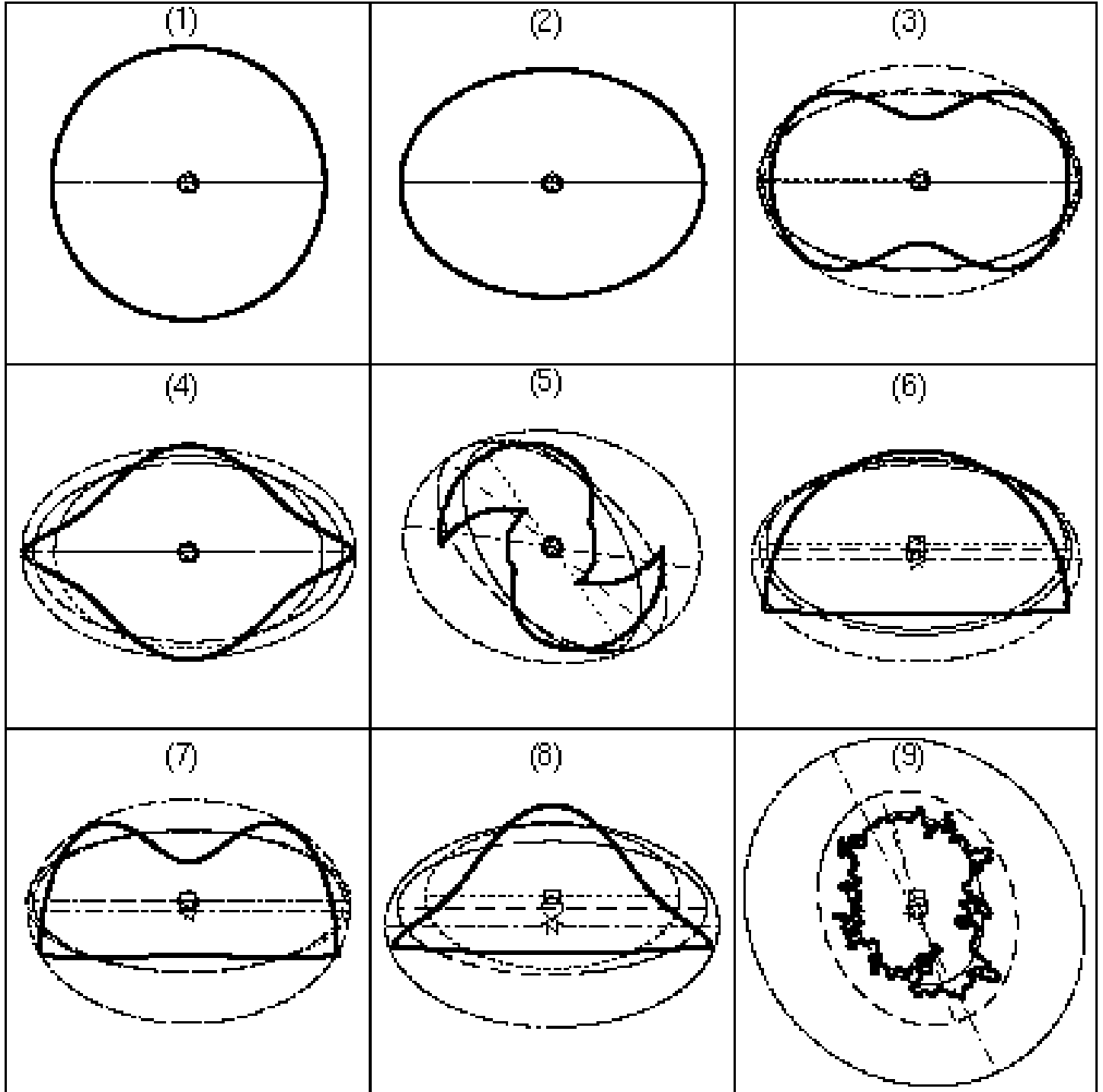


Figure 1. A set of toy contours (solid lines) with their vector and tensor MFs. The vector functionals (A_i, P_i , and χ_i) are shown by the square, circle and star respectively. The tensor functionals are represented by the auxiliary ellipses with corresponding areas and perimeters: (A_A, P_A dotted), (A_P, P_P dashed), and (A_χ, P_χ dashed-dotted). The straight lines passing through the centroids show the orientations of the corresponding auxiliary ellipses.

classified as peculiar type, it is also classified as a barred, irregular, “Magellanic” type low surface brightness galaxy.

4 SPURIOUS EFFECTS

Here we show how discreteness, atmospheric seeing, and noise may affect the accuracy of the measurements of ellipticity and orientation of elliptic images.

4.1 Discreteness

In order to assess the discreteness effect we generate one hundred randomly oriented elliptic profiles (on a 128×128 mesh) with arbitrary position of the centers within a grid. We have compared the results of the measurements with analytic predictions in Fig. 2 where the error in estimated ellipticity is shown as a function of the area of the image. As one might expect the effect is stronger for smaller images and practically disappears for larger images. The four panels in this figure show the deviation of the measured ellipticity from the true one obtained from the scalar (A_S, P_S) and three tensor functionals. The ellipticity derived from the scalar functionals is systematically overestimated for all types of elliptic profiles (from E0 through E7) although the difference becomes smaller for elongated ellipses (E7). The estimate obtained from the area tensor (A_{ij}) has a relatively smaller systematic effect, however the dispersions remain quite large. The least distorted estimate of ellipticity comes from the perimeter (P_{ij}) and the EC (χ_{ij}) tensor. They both slightly underestimate the ellipticity. The elongated contours, e. g. E7, suffer more from discreteness than rounder one, e. g. E0, if derived from the perimeter and EC tensors while the opposite is true if derived from the scalar or area tensor.

4.2 Atmospheric Seeing and Discreteness

An important effect that one must take into account while analyzing galaxy images is the atmospheric seeing. To quantify the effect of seeing on measured parameters we construct profiles as mentioned earlier and smooth them by 2d Gaussian filter. The (real space) width of the filter is taken to be $\sim 1.5''$, an approximate value of typical seeing of 2MASS observation although the actual PSF for the images ranges between $2.5''$ and $3.5''$. The profiles are analyzed as before and the results are shown in Fig. 3. Note that seeing is dominant around the central part of galaxy images which is also prone to the discreteness effect. Therefore interpreting the measurement in this region concentrating only on seeing will be erroneous and the understanding role of discreteness must also be needed. Figure 3 shows their combined effect in ellipticity measurement of various simulated profiles.

The seeing effect make the elliptical images appear rounder and thus reduces the ellipticity of the auxiliary ellipses for all profiles. It is interesting to note that the scalar estimator is slightly improved for rounder images (E0-E3) because the discreteness effects are partly compensated by the seeing. However, all other estimators are affected similarly to the discreteness effect and thus the ellipticity of the elliptic image becomes systematically smaller if estimated by the perimeter or the EC tensor. The area tensor still is

the least affected by the seeing compared to the pure discreteness effect.

4.3 Noise, Atmospheric Seeing, and Discreteness

Noise is an additional source of distortion of the contours of any image. Originally smooth contours begin to wiggle due to noise affecting estimators derived from each functional. For instance, the perimeter and curvature systematically increase with the level of noise. One may speculate that the parameters related to the curvature (in our notations A_χ, P_χ) would be the most affected. However, the EC itself (i.e. χ) does not change at all unless the noise is so high that it breaks the continuity of the contour and split the initial region into two or connect it with another one. The least affected MFs are related to the area and these are A_S, A_A , and P_A .

Figure 4 shows the combined effect of noise, seeing, and discreteness on the ellipticity of the image. The strongest systematic effect is on the scalar quantities (the top left panel). The contour length becomes longer due to wiggling while the area is affected in less systematic way resulting a strong overestimate of the ellipticity, especially for rounder contours. Comparison of Fig. 4 to Fig. 2 and 3 shows that the major effect is due to noise.

The effects of noise increase with decreasing signal to noise ratio S/N. A more detailed analysis shows that locally the ratio of noise (the rms σ_n) to the gradient of the field (Δf) is the most important parameter controlling the distortions of the contour. For gradient we use $\Delta f = |\nabla f \cdot l_g|$ to be explicit in grid unit where l_g is the grid size. To visualize of what is stated above, consider an isophote corresponding to a given brightness level, f_0 , passing through a particular grid point on a 2d mesh. As each grid point on the mesh has a particular brightness level, any other isophote belonging to a level higher or lower than f_0 will go through the inner or outer grids, respectively. In order for the isophote of f_0 to be shifted by the noise to a neighboring outward grid point, the level (or strength) of noise σ_n must exceed the difference of unperturbed levels between the grid points. This shifting of the contour (i.e. distortion due to noise) solely depends on the gradient instead on the brightness level of the isophote.

To elaborate more, we have included a diagram illustrating the dependence of gradient and image noise shown in Fig. 5. Profiles with two different gradients ($\Delta f = 0.5\sigma_n$ and $\Delta f = 1.5\sigma_n$) are considered. The top panels show the unperturbed 1d brightness distribution for lower (top-left) and higher (top-right) gradient profile. The brightness curves are shown in arbitrary unit and the horizontal axis is in grid unit. The longer horizontal line is at the same brightness level for both profiles where the shorter line is drawn at different levels. These lines represent the respective diameters (80 and 50, in grid unit) of the un-perturbed contours shown in the bottom panels. Each of the panels at the bottom contain both un-perturbed and noisy contours placed on top of each other. Thin and thick solid lines are used to show these respective contours. The outer contour is constructed by keeping the same size and brightness level for both profiles (lower horizontal line at the top panels). For the inner contour two different levels (the upper horizontal lines) are chosen but keeping their sizes the same.

With these choices made for contours, on one hand we

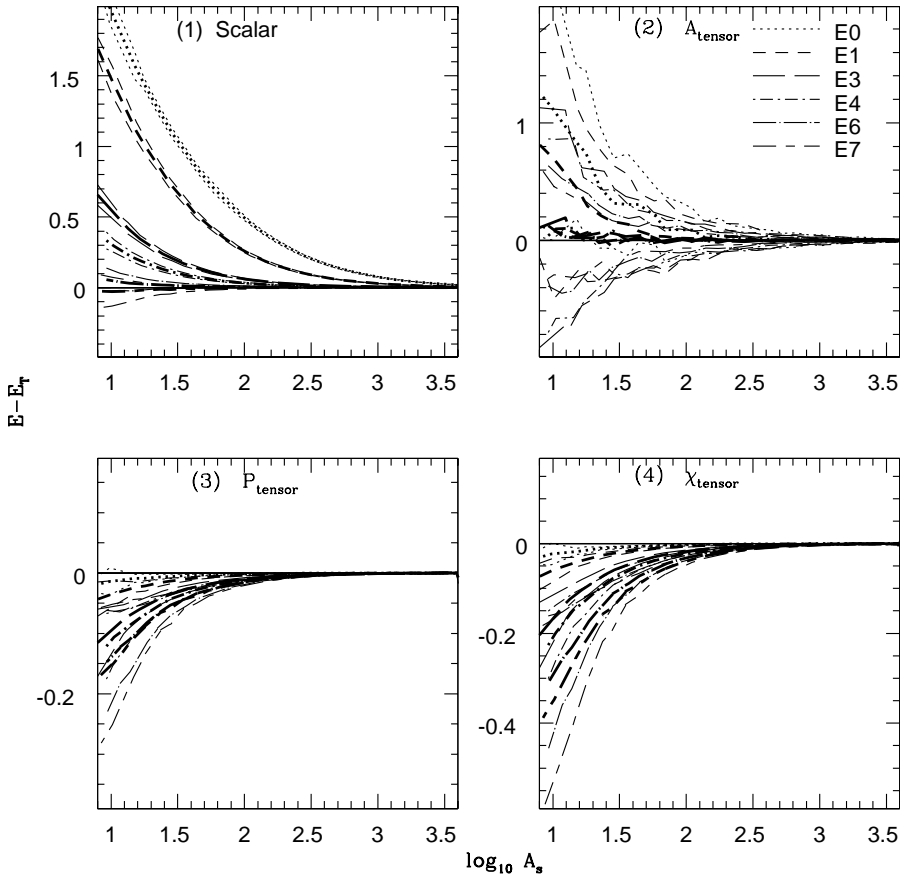


Figure 2. The effect of discreteness on the ellipticity of elliptic contours. The horizontal axis is $\log_{10} A_S$ and the vertical axis is the errors in the measurements of the ellipticity. Different lines mark ellipses with different ellipticities. Heavy lines correspond to the mean; thin lines show one sigma bands.

see that the outer contour of the shallower profile is wiggled more and hence strongly distorted than that of the steeper one. The latter contour appear smooth and close in appearance to its original un-perturbed form. On the other hand we also notice from the appearance of the inner contour (for both profile) that the degree of distortion is not, at all, controlled by brightness level chosen. In spite of its higher level, the low gradient inner contour experiences similar distortion to the lower level outer contour. Contrary to this, the high gradient inner contour appear not only smooth but also similarly perturbed as its outer one. In brief, for low surface brightness profile the noise strength easily gains control over its steepness. Due to the intrinsic shape, the overall profile distribution experience strong influence of noise irrespective of the brightness level. For any given level, noise easily stretches the contour points along the x and y-direction on the 2d mesh and deviates the contours significantly from their original shapes. Comparatively speaking the shifts of the contour points on the mesh for a high brightness profile is less, resulting in smooth contours.

It should be mentioned here that in the discussion above we considered an ideal situation assuming that the gradient remains constant all along the radial direction from center to the edge of the profile. Since our goal is only to illustrate

the significance of gradient-noise relationship, we believe this choice is reasonable. For real galaxy the steepness of brightness distribution varies radially from point to point, being steep at the central part and shallow outward. Due to this reason the real galaxy contours, in general, appear smoother in the center than at the edge.

Any non-circular profiles have different gradients on a given contour at any given level and thus the amount of distortion varies along the contour. A natural assumption is that the average distortion of a contour of arbitrary shape is determined by the mean value of $\sigma_n/\Delta f$. For a linearized elliptic profile

$$f_e(x, y) = F_e - g_e \sqrt{\frac{x^2}{a^2} + \frac{y^2}{b^2}} \quad (15)$$

the mean inverse gradient can be evaluated analytically

$$\left\langle \frac{1}{|\nabla f_e|} \right\rangle = \frac{\pi b}{2g_e E(e)} \quad (16)$$

where e is the eccentricity, b is the semi-minor axis (in grid unit), $E(e)$ is the complete elliptic integral of the second kind, and g_e is the gradient along the semi-major axis.

A rounder and an elongated contour will be distorted similarly if they have the same mean inverse gradient. For an

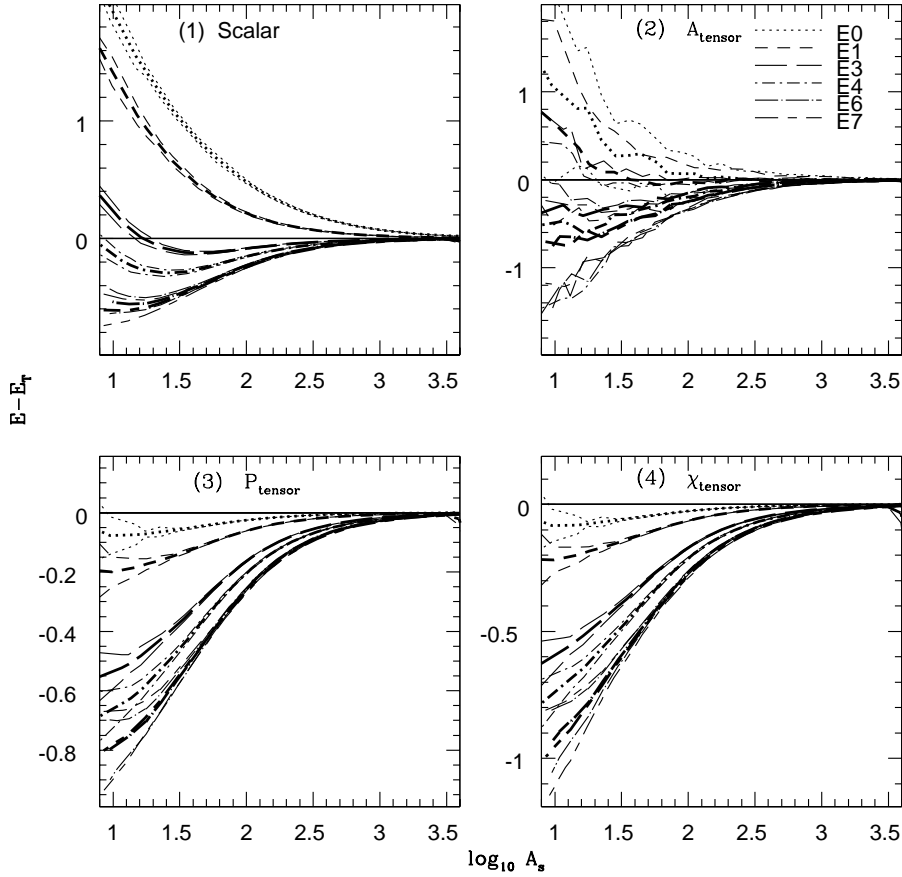


Figure 3. The effect of atmospheric seeing and discreteness on the ellipticity of elliptic contours. The profiles and notations are the same as in Fig. 2.

explicit demonstration and comparison of different profiles at approximately the same distortions, we have generated profiles with different ellipticities but similar slopes. Figure 6 illustrates the dependence of the distortions in areas (left panels) and perimeters (right panels) for circular and elliptic profiles (E7) as a function of $\langle \sigma_n / \Delta f_e \rangle$. For this illustration the images of a medium size $A_S \approx 100$ pixels have been chosen. The relative distortions $((X - X_T) / X_T$ where X is the measurement and X_T is the theoretical, analytic in this case, value of the parameter in question) of the areas and perimeters are approximately linear with $\langle \sigma_n / \Delta f_e \rangle$ at least for $\langle \sigma_n / \Delta f_e \rangle < 2$ for both circular and elliptic profiles. Moreover, the results for a circle and ellipse are approximately similar, which confirms the assumption that the mean inverse gradient is one of the major factors affecting the amount of distortion. Note that only for theoretical model of elliptic profiles it is possible to express the gradient in closed analytic form and can be evaluated exactly. But in more complex cases of real galaxy profiles, analytic form is difficult to obtain and one must calculate the mean inverse gradient numerically.

5 CONTOUR SMOOTHING

The effects of noise on image can be reduced in several possible ways. For example, the widely used method employ smoothing the image/map itself with some known filter function. In our analysis we chose a simple technique, known as the un-equally weighted moving average method, for contour smoothing.

The method is based on replacing the set of contour points by a new set each point of which is placed exactly in the middle of two adjacent points in the original set. This set of new points make a new contour a little smoother than the original one. The procedure is applied iteratively many times depending on the length of the contour and the level of noise. It is worth mentioning that finding the optimal number of smoothing is not a trivial task. The main problem is that without any prior knowledge of the true shape one can in fact smooth a contour so much that it will appear as circular and eventually with further smoothing as a point since this is the ultimate situation.

One possible method of estimating the optimal amount of smoothing could be as follows. One can make an image with known geometry (e.g. elliptical peak or a real galaxy with high S/N ratio) and then distort it by adding real noise taken from the nearby region of the real image in question.

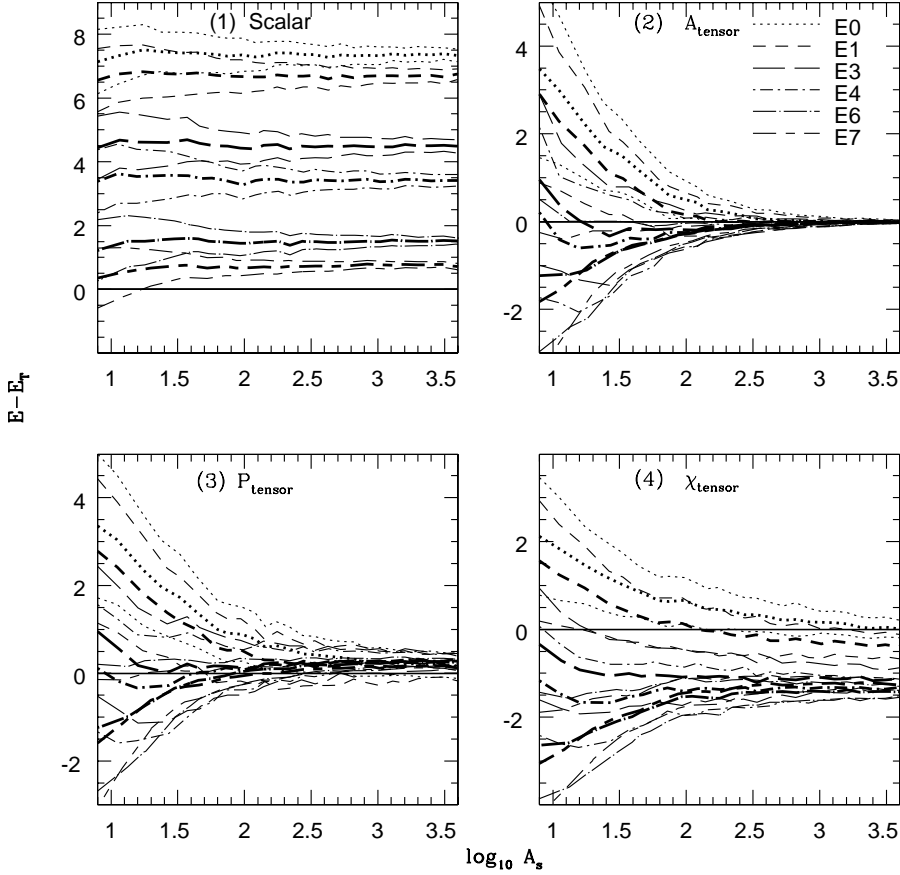


Figure 4. The effect of noise, atmospheric seeing, and discreteness on the ellipticity of elliptic contours. The profiles and notations are the same as in Fig. 2.

Then applying the smoothing technique one can optimize its level on the reference image and use it for the study of the real image. However in this work we simply estimate the effect of Gaussian noise on elliptical profiles reserving a more elaborated technique for the future work.

The goal of smoothing is to restore the initial unperturbed contour as much as possible and measure its morphological parameters. We simulate a hundred realizations of each profile positioning the center randomly inside a pixel, rotating it by a random angle and adding a realization of a Gaussian noise with a specified level of $\sigma_n/\Delta f$. We measure the ellipticities for both distorted and smoothed contours.

The top two rows of panels of Fig. 7 show three selected contours for eight elliptical profiles (E0 - E7) distorted by Gaussian noise along with the auxiliary ellipses. The two bottom rows show the same contours after smoothing. In these rows the auxiliary ellipses practically coincide with the smoothed contours as expected. Figure 8 shows the results of measurement of ellipticities before (only for one realization) and after smoothing (from 100 realizations). The thin dashed lines show the true ellipticity of each profile. These figures show the fact that before smoothing different measures of ellipticity may give different results. The area tensor (A_A, P_A) gives the most accurate estimate of the ellipticity for all types of profiles. The estimate based on the perime-

ter tensor (A_P, P_P) closely follows it. The curvature tensor (A_χ, P_χ) is the least accurate estimator of ellipticity among all three tensorial measures; its accuracy decreases steadily with the increase of the ellipticity. The estimate based on the scalar Minkowski functionals is strongly affected by the noise and is the least accurate for all but very elongated profiles (E6 - E7). Figure 9 shows results for galaxy profiles with shallow brightness distributions.

Contour smoothing results in a considerable improvement of the all estimates. As we mentioned before the number of smoothing steps is determined by the ratio $\sigma_n/\Delta f$ and thus we need to estimate it. We illustrate this using an example of circular contour. The gradient of a circular contour is given by $\Delta f/\Delta r$, where Δf is the difference in brightness levels and Δr is the difference in distances along the radial direction. One can rewrite the gradient as

$$\frac{\Delta f}{\Delta r} = \frac{\Delta f}{\Delta A} \frac{\Delta A}{\Delta r} \quad (17)$$

where A is the area of the contour, $A = \pi r^2$ and ΔA is the difference in area of the corresponding to levels. With $\Delta A/\Delta r = 2\sqrt{\pi A}$, the equation for an estimate of inverse gradient boils down to the following expression

$$\tilde{G} = \frac{\tilde{G}_c}{\sqrt{A}} \frac{\Delta A}{\Delta f} \quad (18)$$

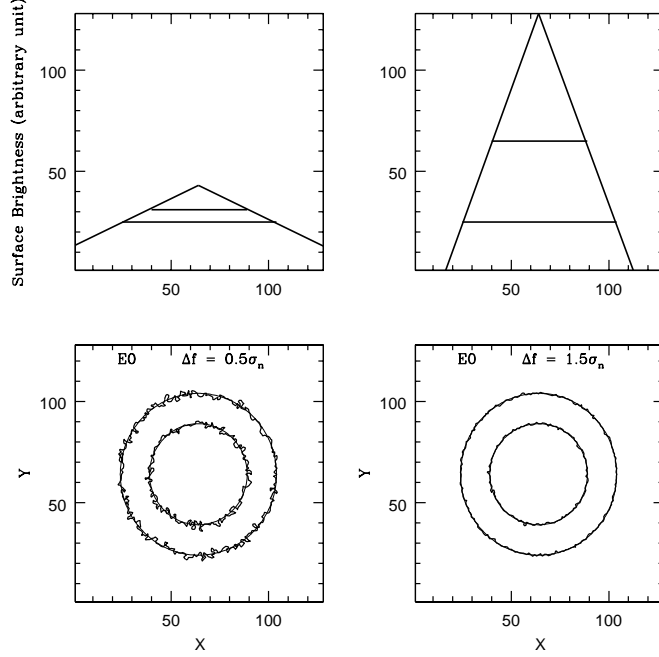


Figure 5. A diagram showing the dependence between the surface brightness gradient and effect of noise. Top panels show un-perturbed 1d distribution curves for both low ($\Delta f = 0.5\sigma_n$, top-left) and high surface brightness ($\Delta f = 1.5\sigma_n$, top-right) profiles. The brightness curves are in arbitrary scale and the horizontal axis is in grid unit. The lower horizontal line show the same brightness level for both profiles and the upper horizontal line is shown at different levels. These lines represent the diameters of the larger (80 grid unit) and smaller (50 grid unit) un-perturbed contours shown by thin solid in the bottom panels. The thick solid line is used to show noisy contours. For details see text.

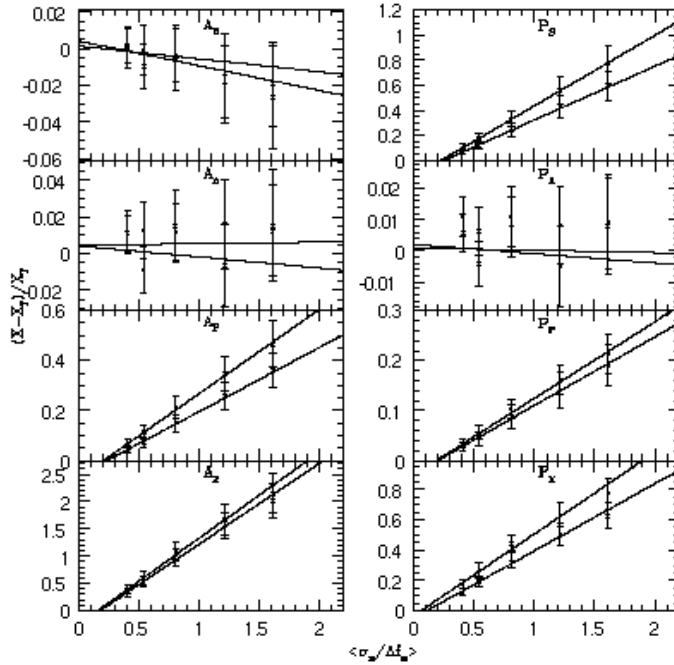


Figure 6. The distortions of area and perimeter for E0 (thin lines) and E7 (thick lines) profiles are shown as a function of $\langle \sigma_n / \Delta f_e \rangle$. The result shown here is obtained from a specific size contour of scalar area $A_S \approx 100$ although it is valid for any contour of arbitrary size. This choice for contour is made for ease of demonstration.

where $\tilde{G} = \Delta r/\Delta f$, and $\tilde{G}_c = 1/(2\sqrt{\pi}) \approx 0.3$. Measuring \tilde{G} gives a reasonable empirical estimate of the inverse gradient $\sigma_n/\Delta f$. Figure 10 shows the results of estimating this quantity for two typical values of $\sigma_n/\Delta f$. The dotted lines show the true value. The estimate of \tilde{G} for rounder contours (from E0 up to E3) overlaps nicely with the true value but becomes less accurate with increasing area as the contour becomes more elongated (from E4 and beyond). At larger area the ΔA is underestimated with the increasing flattening of the contour resulting a lower value (\sim a factor of 2) of \tilde{G} . This corresponds to undersmoothing for larger flattened contours. Since the estimate of shape for these type of noisy contours show better result compared to rounder ones, small amount of smoothing is required for shape recovery and thus undersmoothing is compensated. The measurement of \tilde{G} can be improved if it is calculated for an elliptic contour instead of a circle. We reserve this issue to implement for our future work. The measured \tilde{G} oscillates at smaller area due to discreteness effect that eventually affects the final contour smoothing. This spurious effect is reduced by smoothing \tilde{G} by equally-weighted five points interpolation method. The number of smoothing steps (N_s) is finally achieved by multiplying the smoothed inverse gradient with the contour points (N_p) at each level, i. e., $N_s = \tilde{G} N_p$. The N_s acts as the upper limit of the iterative process (an un-equally weighted moving average method) through which contours get smoothed. Note that the number of steps used to smooth galaxy contours increase from inner smaller regions towards the outer bigger regions. This is well justified by the fact that in the inner region a galaxy has lower inverse gradient (steeper slope) then the outer region (shallower slope). Contours are distorted heavily in the outer region by the noise, traverse longer paths consisting of large number of points and hence invoke higher number of smoothing steps.

All estimates of ellipticity based on tensor functionals converge to one another after smoothing. For sufficiently large images ($\log_{10} A_S > 1.8$, $A_S > 60$ pixel) they also converge to the true values marked by the dashed lines in Figs. 8 and 9, respectively. The estimate of ellipticity based on the scalar functional (A_S, P_S) converge to the true value only for sufficiently elongated ellipses ($E > 2.5$); it is worth noting that the larger the image the faster the convergence. The ellipticity of elongated contours ($E \geq 4$) is estimated more accurately by the scalar functional then by the tensors. Note that an accurate measurement of the ellipticity of circular contours is the most difficult to achieve.

6 EXAMPLES OF GALAXY IMAGES

In order to illustrate the technique we have taken several Near-Infra Red (NIR) images from 2MASS catalogue. These images are $101'' \times 101''$ in size where $1''/\text{pixel}$. The seeing FWHM values for 2MASS are typically in between $2.5''$ and $3.0''$. For details of 2MASS observation and data reduction readers are referred to (Jarrett et al. 2000; Jarrett et al. 2003).

6.1 Elliptic Galaxies

In this present work we only consider the Ks-band (2.2 micron) images since they are less affected by the delete-

rious effects of atmospheric variability (the so-called "airglow" emission) that plague ground-based NIR observations." We choose galaxies of different Hubble types such as NGC5044 (E0), NGC5328 (E1), NGC3608 (E2), NGC3091 (E3), NGC4742 (E4), NGC4008 (E5), NGC5791 (E6), and NGC4550 (E7). Note that the classifications for the galaxies come from optical studies (primarily the RC3, de Vaucouleurs et al. 1991) due to the relatively insensitive separation of Hubble-types at near-infrared wavelengths (Jarrett 2000; Jarrett et al. 2003). The contour of these galaxies having equal area ($A_S \approx 1300$) are shown at the bottom panels in Fig. 11 along with the vector MFs and three auxiliary (tensor) ellipses.

To analyze the galaxies we first measure the ratio of $\sigma_n/\Delta f$ that will allow us to adjust the number of smoothing. Figure 12 shows the results of the measurements: solid lines show the estimates before smoothing and the dashed lines after smoothing. Figure 13 show three contours for each galaxy before (top two rows) and after smoothing (bottom two rows). The auxiliary ellipses for each contour are shown as well.

We next examine the ellipticity of galaxy contours at 30 levels (equally spaced in area in log scale) which covers almost the entire region of each galaxy. We compute the ellipticity of three auxiliary ellipses (E_A, E_P , and E_χ) as well as the ellipticity given by the scalar functional for raw images and then apply smoothing procedure. Figure 14 shows the ellipticity as a function of area A_S ; the top two rows correspond to the unsmoothed images, and the bottom two rows to the smoothed versions. The ellipticity is plotted as a function of area, A_S . We find that the discrepancy between four estimates of ellipticity increases with the growth of the image size corresponding to the decrease in the level. The gradient of the intensity strongly correlate with the level: the lower the level the smaller the gradient (i.e. the greater $\sigma_n/\Delta f$ as shown in Fig. 12). Therefore, the effects of noise are stronger for lower levels corresponding to larger sizes (in A_S) which is in qualitative agreement with the visual impression (Fig. 11). The ellipticity of the images after conntour smoothing is plotted in two bottom rows in Fig. 14. We see a significant reduction of the discrepancy between different estimates. The dashed lines correspond to the measurements of ellipticity of the K_s images at about $3\sigma_n$ level (see e.g. Jarrett et al. (2000) and also the 2MASS Extended Source Full-Resolution Image Server at <http://irsa.ipac.caltech.edu/applications/2MASS/PubGalPS>. Our measurements are in excellent agreement with the results reported in 2MASS catalogue.

All galaxies except E0 and E1 show varying ellipticity that grow from lower values in the interior regions to greater values in the outer parts. Comparing Figs. 8 and 14 we conclude that this growth of ellipticity cannot be explained by seeing and noise effects that become small for $\log_{10} A_S > 1.8$ and thus suggests that it is a real property of NIR galaxies. Note that this trend of ellipticity is in agreement with previous optical results (Leach 1981, Peletier et al. 1990). All but E0 and E1 images show significantly lower ellipticity than in optics.

The orientations of the images are shown in Fig. 15 as a function of the image size A_S . All the rows on the left panel show the results before smoothing and the rows on the right panel after smoothing. The 2MASS position an-

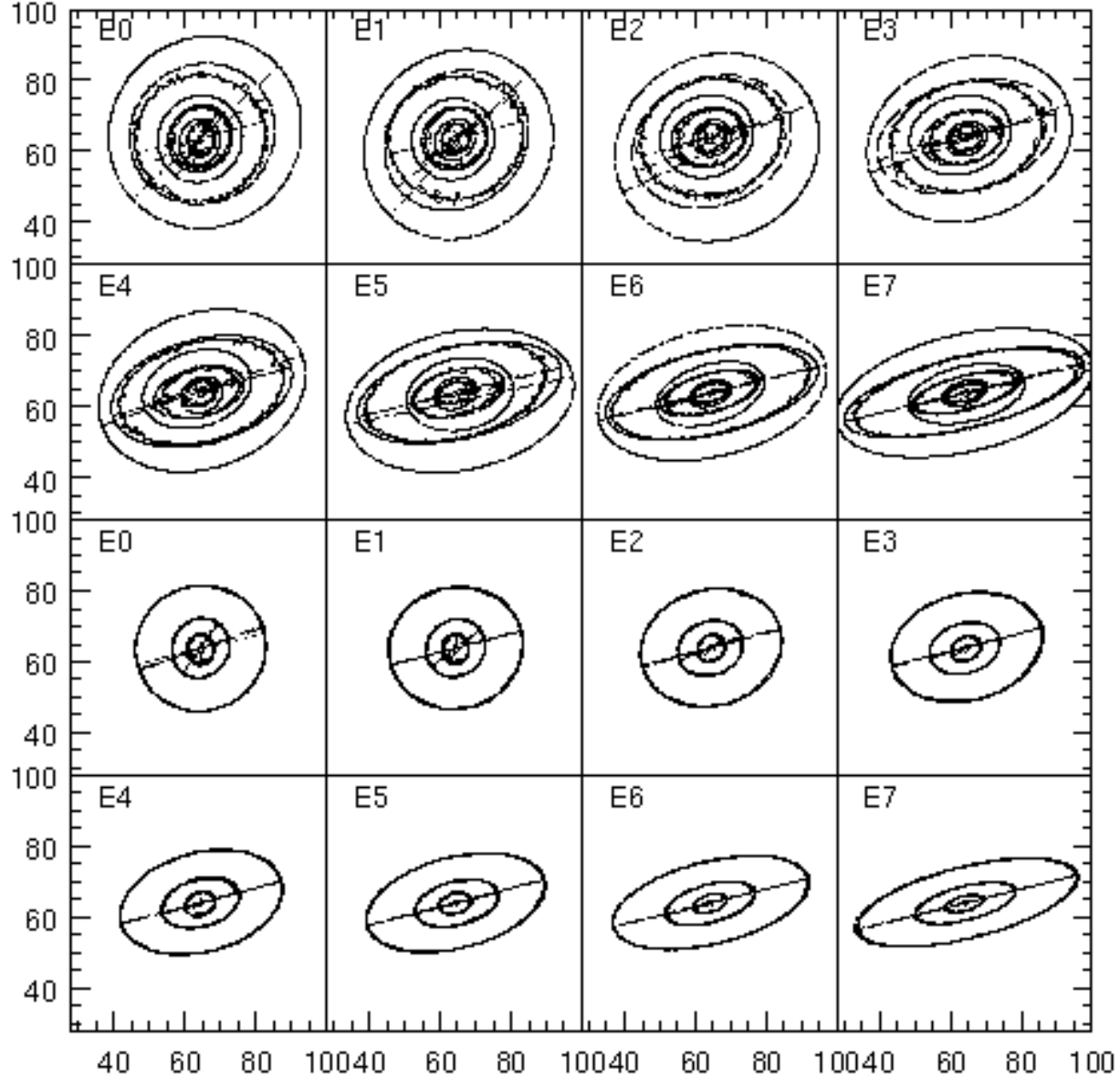


Figure 7. Distortions of isophotal contours by seeing and Gaussian noise are shown for eight elliptical profiles. The top two rows show three contours derived from the linear elliptical profiles with gradient $1.0\sigma_n$ on the largest axis. Along with each contour three auxiliary ellipses are plotted (the line styles are similar as in Fig. 1). Two bottom rows show the contours and the corresponding auxiliary ellipses after smoothing. The scalar areas of the contours are approximately $A_S \approx 50, 200$, and 1000 in grid units.

gles measured at $3\sigma_n$ isophote of K_s band images (measured east of north) are shown on the left panel. We present the result as a difference between our measurement with 2MASS. The horizontal dashed lines correspond to no differences. The vertical dashed lines show the scalar areas in our measurement corresponding to the region enclosed by the $3\sigma_n$ isophote in K_s band. Our measurements are in excellent agreement with 2MASS for all galaxies at the outer regions except E0. While its orientation is within $\sim 10^\circ$ of 2MASS at the outer part, it varies from 30° (where $\log_{10} A_S \sim 2.2-2.4$) to 20° in the central part (where $\log_{10} A_S \sim 2.0$). It should be kept in mind that a perfectly circular contour has no preferred orientation and therefore it is a difficult measure.

If any circular contour gets perturbed by any kind of disturbance it gets deformed from circularity and immediately picks an orientation as a consequence of perturbation. Since the galaxy contours at different levels are affected differently by various spurious effects, we therefore proceed with caution regarding the orientation of the E0 galaxy and state that the variation in isophote orientation would most probably be due to spurious effects and not a true measure. While E2, E4, E5, E6, and E7 galaxies show almost stable orientations throughout the entire regions (variation is within $\pm 4^\circ$), orientations of E1 and E3 galaxies show interesting behavior indicating possible isophotal twists. The E1 orientation grows monotonically ($\sim 10^\circ$) from $\log_{10} \sim 2.7$ towards the

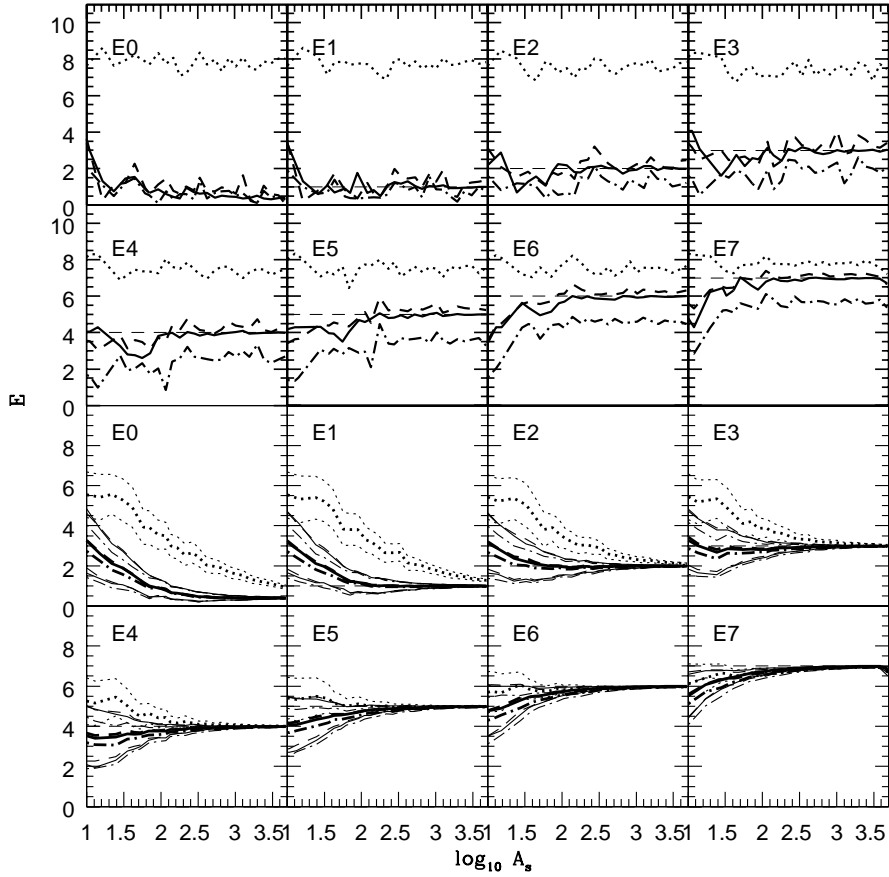


Figure 8. The ellipticity parameter (E) for elliptical profiles shown in Fig. 7 before and after smoothing. The profile brightness distribution has gradient 1σ along the largest axis. The top two panels show the parameter measured from noisy profiles before smoothing. Result from only one realization is shown for demonstration purpose. The bottom two panels show mean and 1σ band for this parameters obtained from 100 realizations after smoothing. Horizontal dashed lines show the true ellipticity. The area, perimeter and curvature ellipses (E_A , E_P , and E_χ) are shown by the solid, dashed, and dashed-dotted lines respectively. The dotted line shows the ellipticity of the scalar ellipse. Heavy lines correspond to the mean; thin lines show one sigma bands.

central part while the E_3 changes $\sim 8^\circ$ around the region where $\log_{10} A_S \approx 2.4 - 2.7$ and gradually decreases towards its center.

6.2 Spiral and Peculiar Galaxies

The images of three early-type spiral galaxies NGC5326 (SAa), NGC4143 (SAB(s)), NGC5006 (SB(r)a) and one peculiar galaxy NGC4004 (Pec) are shown at the top row of Fig. 16. Three selected contours along with the corresponding auxiliary ellipses are shown in the middle (before smoothing) and in the bottom row (after smoothing). For two of the spirals, NGC5326 and NGC4143, smoothing provides both consistent convergence and significant improvement in the shape measurements, similar to the spheroidal galaxy cases. The other two spirals, N5006 and N4004, however, show remarkable inconsistency in the elliptic shape between the inner and outer contours (especially for the case of the scalar functional), suggesting that their projected shape is not simply an ellipse.

The galaxies NGC5326 and NGC4143 have elliptic con-

tours ranging approximately from E_2 in the inner parts to E_5 in the outer parts. The curves are similar to the E_5 - E_6 images of the elliptic galaxies as in Fig. 14. This actually corresponds well to the visual impression: NGC5326 and NGC4143 does look like ellipticals in K_s band (Fig. 16 top row). We present the orientations of these galaxies at the bottom two rows in this figure. The position angle of NGC5326 remains almost stable (within $\sim 4^\circ$) throughout the entire region of the galaxy while the orientation of NGC4143 shows some twist ($\sim 10^\circ$). The 2MASS $3\sigma_n$ angles for these two galaxies are higher than our measurement: for NGC5326 2MASS overestimates by $\sim 4^\circ$ and for NGC4143 by $\sim 8^\circ$.

The galaxies NGC5006 and NGC4004 show very distinctive behavior. First the ellipticities of these galaxies go up and down a couple of times and the estimate of the ellipticity based on the scalar functionals is significantly higher than that of tensor functionals. As we discussed in Sec. 5 the scalar functional coincide with the tensorial estimates for ellipses with sizes greater than about $\log_{10} A_S \approx 1.8$ and ellipticities greater than about E_3 . The scalar ellipses

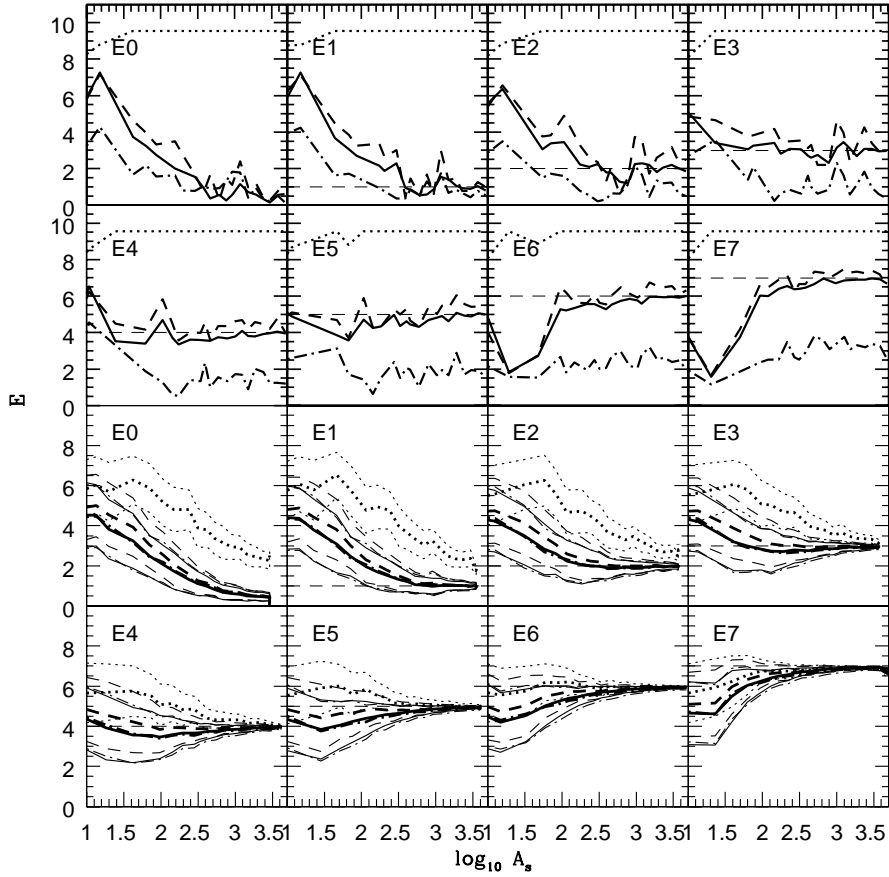


Figure 9. Similar to Fig. 8 except for shallow brightness distribution. The profiles have gradient $0.2\sigma_n$ along the largest axis. This particular shallow distribution is chosen only to highlight the dependence of gradient and noise, and their roles on the measured parameter (E) as well as the significance of contour smoothing. Notice how distorted the profiles becomes owing to low brightness distribution (top two panels). Even though contour smoothing (in bottom two panels) substantially improve recovering shapes for larger elongated contours, for smaller and rounder contours (e.g. $E0 - E2$) it is harder to achieve.

are significantly more elongated than auxiliary ones in the ranges $2 < \log_{10} A_S < 3$ and $E > 3$, where they must coincide with the other estimates if the images were true ellipses (see Fig. 8). We conclude that the discrepancy is real and these parameters can detect elliptic shapes of these images that appear different than previous results.

The change in orientation of the auxiliary ellipse is also much stronger than in the case of elliptic galaxies. Both of these galaxies show huge variations in orientation ($\sim 40^\circ$) towards the central region. This change in the direction of isophote might be used as a probe to isolate early types galaxies from late types. Note that the orientations of these galaxies are overestimated by our measurement compare to $3\sigma_n$ angles of the 2MASS: $\sim 3^\circ$ for NGC5006 and $\sim 5^\circ$ for NGC4004. We show the differences in orientations for these galaxies in Fig. 17 after reducing by a factor of 2. It is remarkable that two simple characteristics the ellipticities and the orientations of the auxiliary ellipses measured as a function of the image size are able to detect varied elliptical shapes. We will elaborate this issue in a forthcoming paper.

7 SUMMARY

We have derived and tested a set of morphological parameters that can be used for quantification of the geometry and topology of two-dimensional images such as galaxies, clusters, and superclusters of galaxies. We have demonstrated their efficiency by measuring the ellipticity and orientations of hundreds of simulated distributions and a dozen of 2MASS images.

We begin with the construction of a set of contours of constant intensity at chosen levels for an image given as a pixelized map. To build a contour we use a linear interpolation scheme as described in (Shandarin et al. 2002). Then we compute three scalar, three vector, and three tensor (rank 2) Minkowski functionals. Three scalar MFs are the area (A_S), perimeter (P_S), and Euler characteristic (χ) of the region within the contour. Two vector MFs A_i and P_i define two centroids which are the center of area of the region and the center of mass of the contour assuming that the linear density of the boundary are uniform. The third vector functional χ_i defines the center of mass of the contour with the linear mass density proportional to the curvature of the

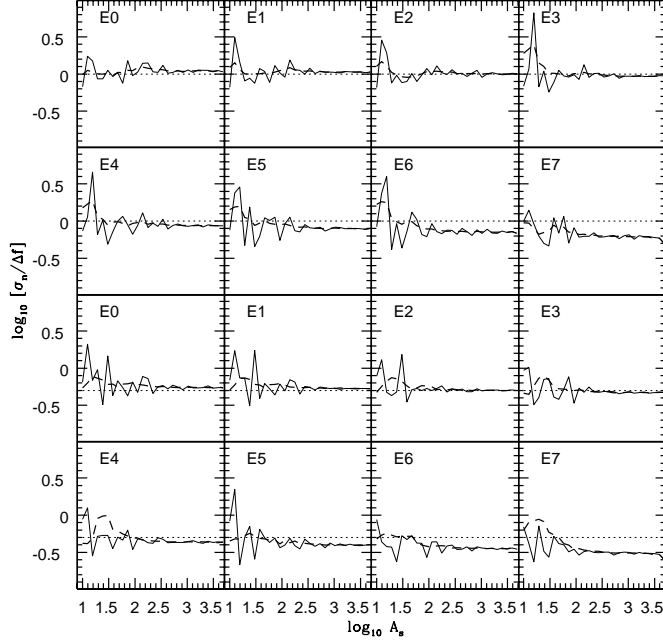


Figure 10. The inverse gradient $\sigma_n/\Delta f$ as a function of $\log_{10} A_S$ measured for eight elliptical profiles shown in Fig. 7. The top two rows show the case $\sigma_n/\Delta f = 1$ and the bottom two correspond to $\sigma_n/\Delta f = 0.5$. The dotted lines show the true value of $\sigma_n/\Delta f$.

contour. In addition, we compute three tensors of the second rank which are analogous to the inertia tensors: two assume that the surface density of the area and the linear density of the boundary are uniform and the third one assumes that the boundary density is proportional to the curvature of the boundary (Beisbart 2000).

We transform the measured vector and tensor components into parameters of three auxiliary ellipses: one having exactly the same vector and tensor MFs as the region within the contour (eqs. 4 and 7), another as the uniform contour (eqs. 5 and 8) and the third one as the contour weighted at every point by its curvature (eqs. 6 and 9). The vector MFs (A_i , P_i , and χ_i), the corresponding region centroids, also represent the corresponding auxiliary ellipse centroids. This transformation conserves morphological information and provides more homogeneous set of characteristics: four areas (A_S, A_A, A_P, A_χ) and four perimeters (P_S, P_A, P_P, P_χ), corresponding to the contour itself and to the auxiliary ellipses. Finally, the MFs provide the position angle directions of the corresponding auxiliary ellipses. One useful property of these parameterization is that in the case of a true elliptic region all areas are the same and equals the area of the region itself. Same is true for the perimeters and the axes.

Here we studied in detail the ability of the method to measure the ellipticities and orientations of contours. We have tested the effects of grid, atmospheric seeing, and noise on the described morphological parameters of hundreds of simulated elliptic profiles from E0 to E7. We find that for real data, represented by K_s -band imaging of galaxies from 2MASS, the background noise is the dominant factor. In order to reduce it we introduced a simple iterative technique for smoothing the perturbed contours and tested it on a

set of elliptic profiles. We show that our method of contour smoothing greatly reduces the effect of image noise, allowing accurate and rapid convergence of the shape measurements.

As an illustration, we applied the technique to eight images of elliptic (NGC5044, NGC5328, NGC3608, NGC3091, NGC4742, NGC4008, NGC5791, and NGC4550), three spiral (NGC5326 (SAa), NGC4143 (SAB(s)), NGC5006 (SB(r)a)) and one peculiar/irregular (NGC4004(Pec)) galaxy taken from the 2MASS catalogue.

We investigated the performance of the method with surface brightness, ranging from the inner nuclear regions out to the faintest contours (Fig. 14, 15, and 17). We show that the ellipticities of all but NGC5044 and NGC5328 galaxies grow with the size and reach the ellipticity reported in Jarrett (2000) and 2MASS catalogue. The measured elliptic shape (ellipticity and orientation) is consistent for all four MF derivations, unmistakably proving that the projected shape of these galaxies is elliptic as seen in the 2-micron window.

Although our sample is small, the results for the asymmetric galaxies (NGC5006, NGC4004) in comparison with the spheroidal and normal disk spirals, suggest that our method can be used as a powerful discriminant of normal, smooth galaxies and those possessing large scale structures and asymmetries (e.g., bulges, bars, disk warps, rings, one-armed spirals, etc). The four ellipticities derived from the MFs, as a function of size, show quite different patterns from elliptic galaxies. Combined with the position angles they clearly distinguish non-elliptic images. We would like to stress that the main goal of this study was the measurement of ellipticities and orientations of elliptic galaxies. We will report more on the discriminating power of this technique in the forthcoming papers. The technique is compu-

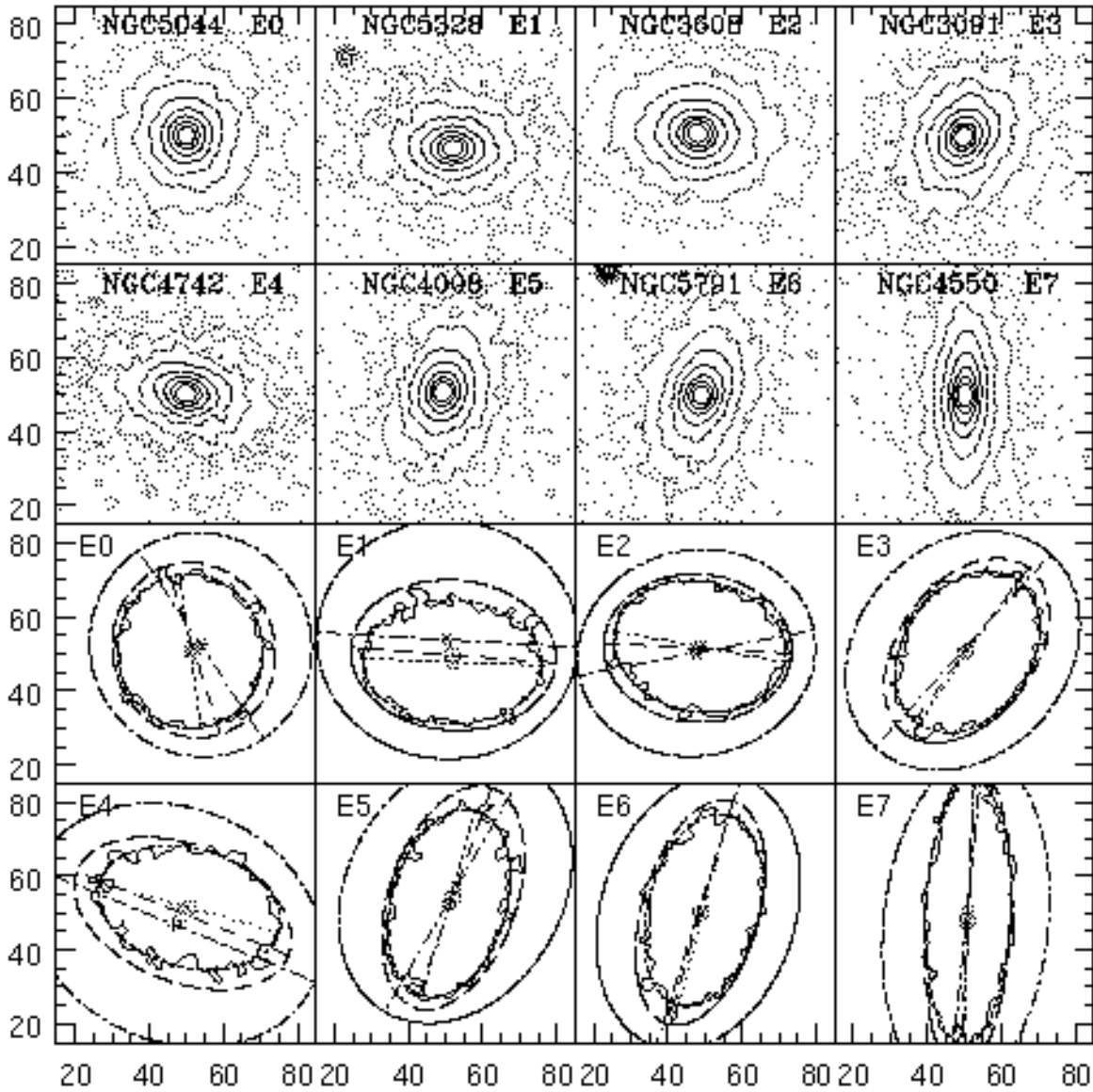


Figure 11. Eight K_s band galaxy images from 2MASS catalogue (optically classified as ellipticals) are shown in two top rows. Nine contours correspond to the areas $20 \times 2^{n-1}$ in grid units ($n = 1, \dots, 9$). Two bottom rows show the contours corresponding to the area $A_S \approx 1300$ along with the centroids and auxiliary ellipses marked similarly as in Fig. 1.

tationally very efficient (Shandarin et al. 2002) and can be applied to the analysis of large data sets like SDSS. We shall report the results of a larger sample of 2MASS galaxies in the following paper (Rahman & Shandarin 2003).

Acknowledgments: We are thankful to our referee Tom Jarrett for his valuable comments and suggestions. We are also thankful to Robert Cutri and Chris Miller for useful communication. NR thanks to Barbara Twarog, Bruce Twarog, and Hume Feldman for valuable discussion. SFS acknowledges the useful discussion during the workshop at the Aspen Center for Physics in June 2002. We acknowledge the use of 2MASS galaxy images from 2MASS data archive

and also acknowledge the support of the GRF 2002 grant at the University of Kansas.

REFERENCES

- Beisbart C., 2000, PhD Thesis, Ludwig-Maximilians-Universität, München
- Beisbart C., Buchert T., Wagner H., 2001, *Physica A*, 293, 529B
- Beisbart C., Valdarnini R., Buchert T., 2001, *A&A*, 379, 412
- Carter D., Metcalfe N., 1980, *MNRAS*, 191, 325
- Crofton M. W., 1968, *Phil. Trans. Roy. Soc. London*, 158, 181
- de Vaucouleurs G., de Vaucouleurs A., Corwin H. G. Jr., Buta

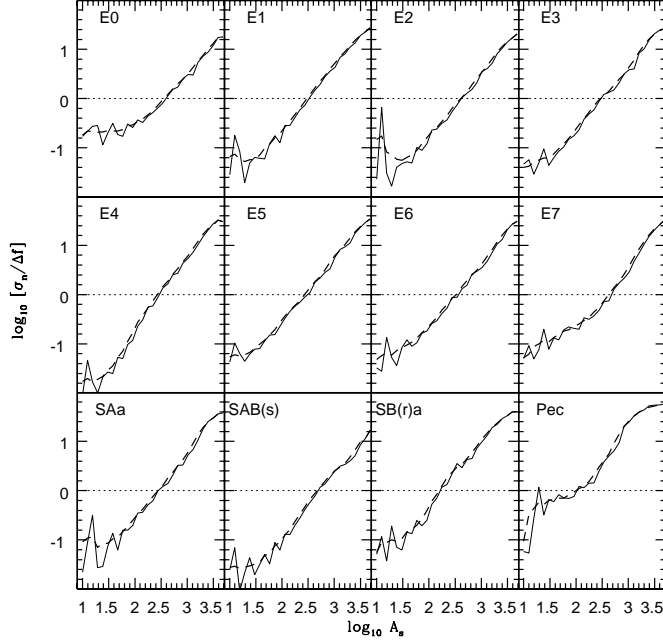


Figure 12. The inverse gradient $\sigma_n/\Delta f$ as a function of $\log_{10} A_s$ measured for eight galaxies from 2MASS catalogue (Fig. 11). The solid and dashed lines correspond to the raw and smoothed images respectively. The dotted line marks $\sigma_n/\Delta f = 1$.

R., Paturel G., Fouqué P., 1991, Third Reference Catalogue of Bright Galaxies (Berlin: Springer) (RC3)

Hadwiger H., 1957, Vorlesungen über inhalt, oberfläche und Isoperimetrie, Springer-Verlag, Berlin

Hobson M. P., Jones A. W., Lasenby A. N., 1999, MNRAS, 309, 125

Jarrett T. H., 2000, PASP, 112, 1008

Jarrett T. H., Chester T., Cutri R., Schneider S., Skrutskie R., Huchra J. P., 2000, ApJ, 119, 2498

Jarrett T. H., Chester T., Cutri R., Schneider S., Skrutskie R., Huchra J. P., 2003, AJ, 125, 525

Kerscher M., Schmalzing J., Retzlaff J., Borgai S., Buchert T., Gottlöber S., Müller V., Plionis M., Wagner H., 1997, MNRAS, 284, 73

Kerscher M., Mecke K., Schmalzing J., Beisbart C., Buchert T., Wagner H., 2001(a), A&A, 373, 1

Kerscher M., Mecke K., Schuecker P., Bhringer H., Guzzo L., Collins C. A., Schindler S., De Grandi S., Crudace R., 2001(b), A&A, 377, 1

Leach, R. 1981, ApJ, 248, 485

Longuet-Higgins M. S., 1957, Phil. Trans. Roy. Soc. London, A, 249, 321

Mecke K. R., Buchert T., Wagner H., 1994, A&A, 288, 697

Minkowski H., 1903, Math. Ann., 57, 447

Mukundan, R. & Ramakrishnan, K.R. 1998, Moment Functions in Image Analysis. Theory and Applications. World Scientific, Singapore

Novikov D., Feldman H. A., Shandarin S. F., 1999, Int. J. Mod. Phys., D8, 291

Novikov D., Schmalzing J., Mukhanov V. F., 2000, A&A, 364, 17

Peletier, R. F., Davis, R. L., Illingworth, G. D., Davis, L. E., & Cawson, M. 1990, AJ, 100, 1091

Rahman N., & Shandarin S. F. 2003, in preparation

Sahni V., Sathyaprakash B. S., Shandarin S. F., 1998, ApJ, 495, L5

Schmalzing J., Buchert T., 1997, ApJ, 482, L1

Schmalzing J., Gorski K. M., 1998, MNRAS, 297, 355

Schmalzing J., Buchert T., Melott A. L., Sahni V., Sathyaprakash B. S., Shandarin S. F., ApJ, 526, 568

Shandarin S. F., 2002, MNRAS, 331, 865

Shandarin S. F., Feldman H. A., Xu Y., Tegmark M., 2002, ApJS, 141, 1

Sheth, J., Sahni, V., Shandarin S. F., Sathyaprakash, B. 2003, to be published in MNRAS, astro-ph/0210136

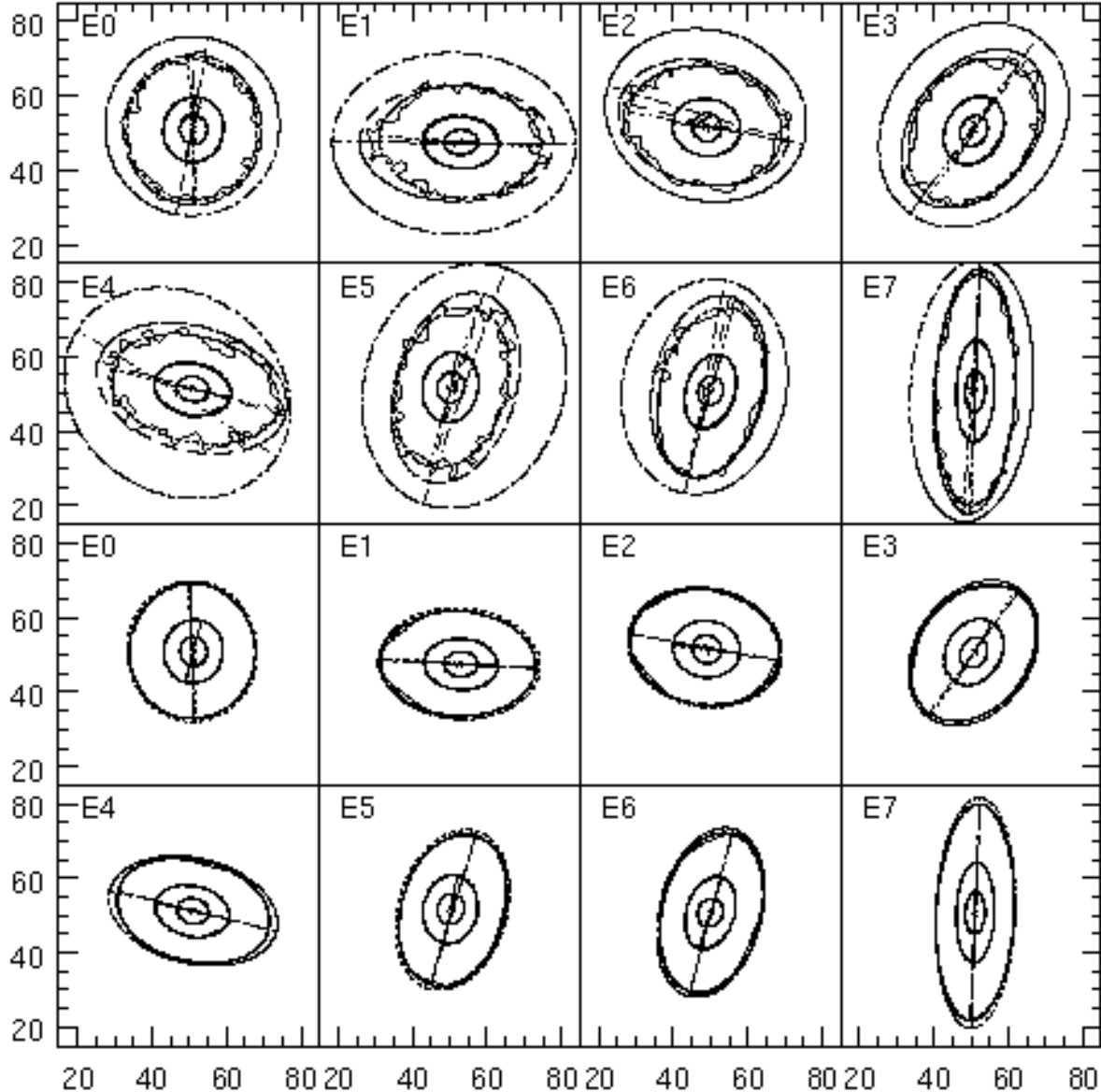


Figure 13. The contours of eight galaxy images from 2MASS catalogue shown in Fig. 11. Three contours corresponding to the areas $A_S \approx 50, 200$, and 1000 in grid units. Two bottom rows show the same contours after smoothing. The lines and legends are similar as in Fig. 1.

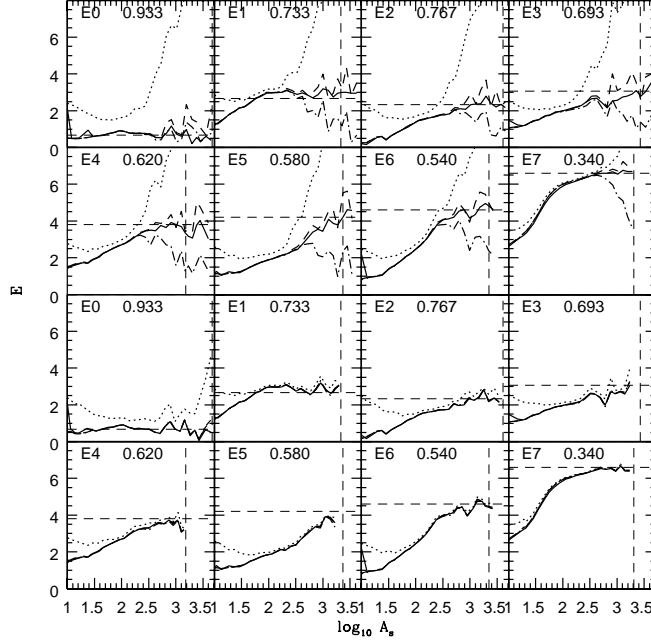


Figure 14. The ellipticity of eight galaxies shown in Fig. 11 as a function of $\log_{10} A_S$. The ellipticities of the area, perimeter, and curvature ellipses are shown along with the ellipticity of the scalar ellipse. The line styles are similar as in Fig. 8. The raw images have been used in the top two rows. The bottom two rows show the ellipticities of smoothed contours. The horizontal dashed lines mark the $3\sigma_n$ isophote ellipticities of these galaxies given by the 2MASS catalogue. The vertical dashed lines show the scalar areas in our measurement corresponding to the region enclosed by the $3\sigma_n$ isophote in K_s band. The numbers at top right on each row are $3\sigma_n$ isophote axis ratios reported in the 2MASS catalogue.

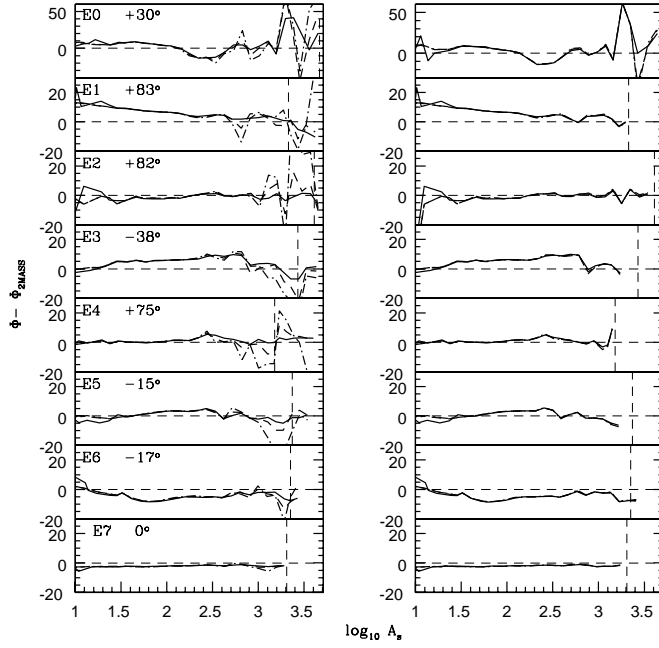


Figure 15. The orientations of three auxiliary ellipses as a function of $\log_{10} A_S$. The rows on the left panel show the orientation of raw images while those on the right show the orientations after smoothing. The horizontal dashed lines show the difference between the orientation of each of these ellipses with the 2MASS $3\sigma_n$ isophote position angle (shown at the top on the left panel). The vertical dashed lines have similar meaning as in Fig. 14. Note that the vertical limit for E0 galaxy is different than all other galaxies.

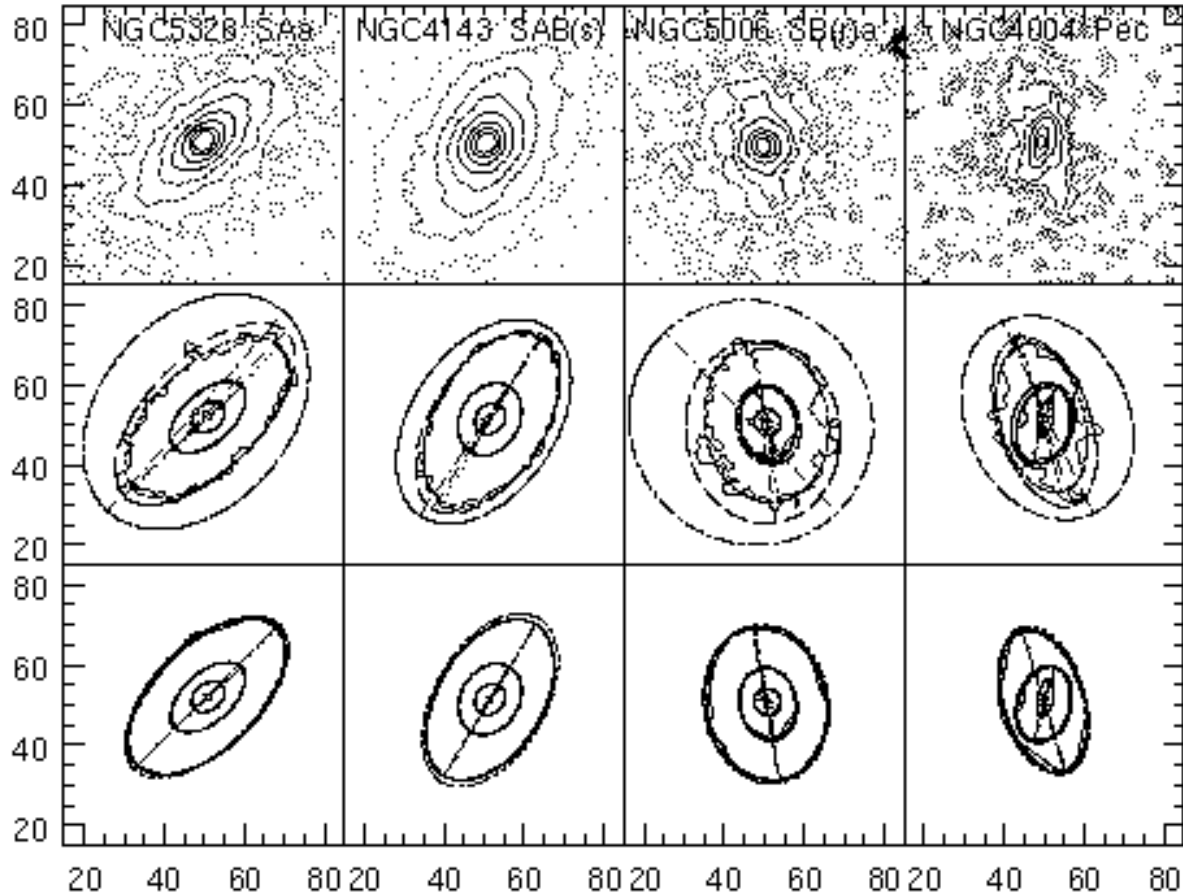


Figure 16. The contour plot of four galaxies optically classified as spiral and peculiar are shown in the top row. The contours correspond to the areas $20 \times 2^{n-1}$ in grid units. Three contours with areas $A_S \approx 50, 200$, and 1000 in grid units along with the centroids and auxiliary ellipses are shown in the middle row. The bottom row shows the the contours after smoothing. The line and legend styles are similar as in Fig. 1.

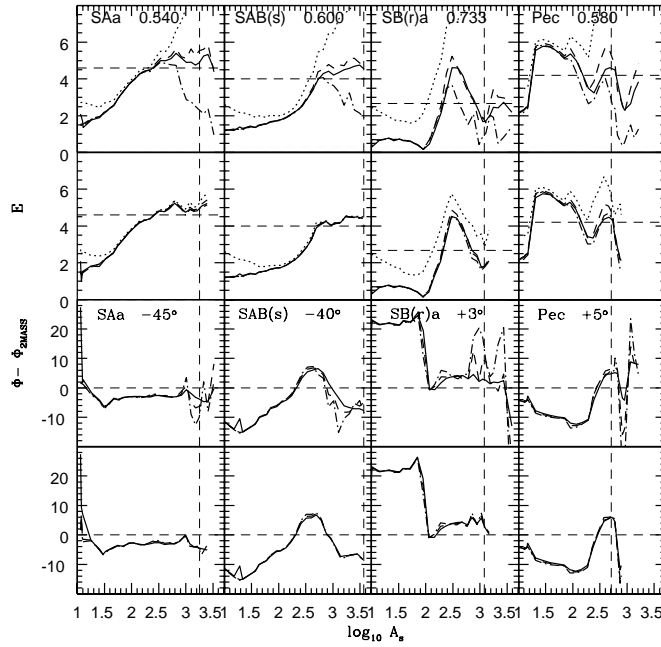


Figure 17. The ellipticity of the four galaxies from Fig. 16 are shown as a function of $\log_{10} A_S$ before (top row) and after smoothing (second row). The numbers at the top row are $3\sigma_n$ isophote axis ratios. The orientation of the auxiliary ellipses are shown in the two bottom rows: before (second row from the bottom) and after smoothing (the bottom row). The $3\sigma_n$ isophote orientations are shown at the row second from the bottom. The horizontal dashed lines in the top two rows and the vertical dashed lines in all rows have similar meaning as in Fig.14. The horizontal dashed lines at the bottom two rows have similar meaning as in Fig. 15. Note that the differences in orientation for SB(r)a and Pec galaxies has been reduced by a factor of 2 for demonstration.